ELSEVIER

Contents lists available at ScienceDirect

Earth and Planetary Science Letters

journal homepage: www.elsevier.com/locate/epsl



Nutrient transition metals in a time series of hydrothermal vent fluids from Main Endeavour Field, Juan de Fuca Ridge, Pacific Ocean



Guy N. Evans*, William E. Seyfried Jr., Chunyang Tan

Department of Earth and Environmental Sciences, University of Minnesota, Minneapolis, MN, 55455, USA

ARTICLE INFO

Article history: Received 25 April 2022 Received in revised form 1 November 2022 Accepted 28 November 2022 Available online 7 December 2022 Editor: B. Wing

Keywords: seafloor hydrothermal long-term observation Pacific Ocean early life Ocean Networks Canada

ABSTRACT

Cabled deep-sea observatories can deliver continuous power and communications linkages to seafloor instruments and sampling devices. Building on this capability, a nine-month time series of hydrothermal vent fluids was recently collected from the well-studied Main Endeavour Field on the Juan de Fuca Ridge (northeast Pacific Ocean) using a novel remotely triggered vent fluid sampling system connected to Ocean Network Canada's NEPTUNE observatory (Seyfried et al., 2022). These samples exhibit very low Mg concentrations (Mg = 0.19–3.07 mmol/kg), indicative of little-to-no contamination by ambient seawater, providing excellent insight into sub-seafloor hydrothermal processes. Here, we present analyses of these samples for transition metals identified as biological nutrients (V, Cr, Mn, Fe, Co, Ni, Cu, Zn, Mo, Cd, and W) and identify possible controlling processes.

Overall, nutrient transition metal concentrations in collected samples reflect dynamic responses to subtle deep-seated and near-surface changes in the hydrothermal system. Roughly two months into the deployment, inmixing of a Mg- and sulfate-rich fluid is decoupled from observed changes in vent fluid temperature but coincides with noticeable decreases in fluid Co and Mo concentrations, likely indicating subtle or more deep-seated cooling of the system and subsurface deposition of these temperaturesensitive metals. Several months later, a ~20 °C drop in vent fluid temperature from 304 °C to 280-285 °C over \sim 20 hours is accompanied by \sim 90% decreases in Cu, Zn, and Cd concentrations and an additional decrease in Mo attributable to precipitation of metal sulfides, presumably in the shallow subsurface. Relative stability in concentrations of other metals (V, Cr, Mn, Ni, W) suggests more deeply seated higher-temperature controls, though covariations in Cr and Ni concentrations decoupled from vent fluid temperature suggest subtle, temporally variable lithologic controls. Molybdenum concentrations (29-220 nmol/kg) are higher than expected based on previous analyses of seafloor hydrothermal vent fluids and do not reflect contamination by modern Mo-rich seawater. This finding has implications for understandings of hydrothermal Mo delivery to the ocean, relevant to hypotheses about the evolution of Mo-dependent biological pathways among early life forms in anoxic and Mo-poor ocean environments thought to be prevalent throughout the Archean Eon.

© 2022 Elsevier B.V. All rights reserved.

1. Introduction

Seafloor hydrothermal fluids affect ocean chemistry, with inputs mediated by hydrothermal plumes (German et al., 1991; Alt, 1995; German and Seyfried, 2014; Findlay et al., 2015; Gartman and Findlay, 2020; Kleint et al., 2022). Hydrothermal plumes have been shown to transport materials long distances (Wu et al., 2011; Nishioka et al., 2013; Fitzsimmons et al., 2014; Resing et al., 2015; Roshan et al., 2016; Fitzsimmons et al., 2017) and enhance biological activity at regional-to-global scales (Tagliabue et al., 2010;

Ardyna et al., 2019; Schine et al., 2021). Recent mapping of trace elements in deep open ocean waters has identified hydrothermal sources of dissolved Fe, Mn, and Zn and particulate V, Cr, Mn, Fe, Co, Cu, and Zn (SCOR Working Group, 2007; GEOTRACES, 2021).

Hydrothermal vents have also been invoked as sources of transition metal nutrients necessary for life's origin and subsequent evolution, either globally (Da Silva and Williams, 2001; Saito et al., 2003; Moore et al., 2017, 2018), or in vent-centered microenvironments (e.g., Nitschke and Russell, 2009; Weiss et al., 2016). Early life processes requiring transition metals include methanogenesis, which currently requires Fe, Co, Ni, and Mo or W, and nitrogen fixation, which requires Mo, V, or Fe (Bishop and Joerger, 1990; Nitschke and Russell, 2009; Weiss et al., 2016; Moore et al., 2017). Transition metals identified as essential biological nutrients include

^{*} Corresponding author.

E-mail address: gevans@umn.edu (G.N. Evans).

V, Cr, Mn, Fe, Co, Ni, Cu, Zn, Mo, and possibly Cd and W (Williams and Rickaby, 2012).

Despite such hypotheses, knowledge of nutrient transition metals in seafloor vent fluids remains relatively poor. While experimental studies and routine measurements have provided insight into the behavior of Mn, Fe, Zn, and Cu (Seewald and Seyfried, 1990; Seyfried and Ding, 1993; Pester et al., 2011; Xing et al., 2022), data on other nutrient transition metals remain sparse, despite some intermittent progress (e.g., Trefry et al., 1994; Metz and Trefry, 2000; Seyfried et al., 2003; Schmidt et al., 2007, 2011; Findlay et al., 2015; McDermott et al., 2018; Evans et al., 2020).

Here, we present analyses of nutrient transition metals (V, Cr, Mn, Fe, Co, Ni, Cu, Zn, Mo, Cd, and W) in a nine-month time series of hydrothermal vent fluids collected from Main Endeavour Field (MEF) on the Juan de Fuca Ridge (northeast Pacific Ocean) using a recently developed remotely triggered sampling device (Seyfried et al., 2022). Samples exhibit little-to-no seawater contamination, providing unprecedented temporal insights into dynamic subseafloor processes through their effects on vent fluid transition metal concentrations. Trace element partitioning between fluid samples and metal-rich precipitates that formed as samples cooled provides insight into analogous processes occurring in the first several meters of the buoyant hydrothermal plume (e.g., Findlay et al., 2015), as hydrothermal fluids cool and inject particles into the water column. Time series studies, such as that presented here, provide insight into the dynamics of hydrothermal systems and offer invaluable informational inputs to biogeochemical models of nutrient transition metals in deep-sea marine environments.

2. Study area

Main Endeavour Field (47° 57' N, 129° 06' W, \sim 2200 m water depth) is located along the western edge of the axial valley that bisects the central, shallowest section of the Endeavour Segment of the Juan de Fuca Ridge, off the west coast of North America (Tivey and Delaney, 1986; Delaney et al., 1992; Fig. 1). Motivated in part by its proximity to major scientific research and port facilities in Canada and the United States and additional hydrothermal interactions with continentally derived sediment, MEF has been the subject of intense scientific research beginning with the initial discovery papers of Delaney et al. (1992) and Robigou et al. (1993). Since 2009, this primarily ship-based research has been enhanced by instrumentation linked to Ocean Network Canada's NEPTUNE cabled observatory (https://oceannetworks.ca/).

Main Endeavour Field vent fluids, which exhibit maximum temperatures > 350 °C (e.g., Butterfield et al., 1994), are characterized by high (1.8–3.4 mmol/kg) concentrations of isotopically light (δ^{13} C = -48.4 – -55.0) methane attributed to thermogenesis from organic matter in continentally derived sediment (Lilley et al., 1993). Hydrothermal fluid pH measured at 25 °C (pH_{25°C} = 4.3–4.5, Butterfield et al., 1994) is also somewhat higher than comparable basalt-hosted vent fluids from unsedimented mid-ocean spreading centers, a difference attributed to pH buffering by NH₃/NH₄⁺ likewise derived from thermogenesis (Tivey et al., 1999).

Butterfield et al. (1994) identified a north-south gradient of decreasing salinity across the vent field in vent fluids collected in 1984–1989, attributing this observation to phase separation at shallower pressures toward the southern end of the field. In 1999, a seismic swarm and inferred dike intrusion (Johnson et al., 2000) lead to anomalously large differences in vent fluid salinity consistent with phase separation at near-seafloor pressures (220 bar) (Seyfried et al., 2003). However, fluids collected in 2000 more closely resembled pre-event vent fluid chemistry (Seewald et al., 2003). The extensive scientific record concerning the MEF system, including trace metal analyses of 1999 vent fluids (Table 1), il-

lustrates the dynamics of the MEF system on longer time scales and adds context to the more subtle variations in hydrothermal processes and associated vent fluid characteristics presented here.

3. Methods

3.1. Sample acquisition

Samples were collected using a newly developed remotely operated serial sampler comprising 12 isobaric gas-tight fluid samplers similar to those of Seewald et al. (2002) connected to a single sampling snorkel (Seyfried et al., 2022; Fig. 2). All wetted components are constructed of grade 2 titanium or PEEK, precluding corrosion in high temperature fluids and/or seawater. The sampler was deployed at the MEF South BARS site of the NEPTUNE observatory (Fig. 1, 3), a small \sim 1 m-high hydrothermal chimney deposit (47° 57' 53" N, 129° 05' 56" W, 2188 meters below sea level) a few meters away from the historically named "Smoke & Mirrors" (S&M) deposit structure of Delaney et al. (1992), collecting nine 160 ml fluid samples between October 2019 and May 2020. Further details about the sampler's design and initial deployment and major element chemistry of collected fluid samples can be found in Seyfried et al. (2022).

Vent fluid samples were maintained at seafloor pressures (220 bar) prior to laboratory sampling and analysis at University of Minnesota. This pressure was confirmed immediately prior to pH, gas, and total sulfide analysis by connecting the back pressure fluid reservoir to a Teledyne 260D ISCO syringe pump (Teledyne ISCO, Lincoln NE, USA). Temperature was obviously not maintained during sampling, leading to precipitation of solid particles within the samplers. Sampler precipitate (a.k.a. "dregs") fractions were collected on 0.2 µm pore-size polysulfone filters. Additional samples were collected of mineralization that accumulated on the sampler snorkel head throughout the nine-month deployment and similar mineralization that grew on a temperature-pH-redox sensor of the type described in Ding and Seyfried (2007) deployed in the same vent orifice the year prior. In both cases, minerals grew on solid titanium in direct contact with venting fluid (Fig. 4).

3.2. Hydrothermal fluid chemistry

Vent fluid temperature, Cl, H₂S, H₂, pH (at 25 °C) and other major chemical components are as reported in Seyfried et al. (2022). Briefly, Cl and sulfate were determined by ion chromatography (Dionex ICS-5000, Thermo Fisher Scientific, Waltham, MA, USA), H₂S by iodometric titration, H₂ by gas chromatography (Agilent 6980, Santa Clara, CA, USA), and pH (NBS scale, at 25 °C) by Thermo-Ross pH electrode calibrated with pH 4 (K-biphthalate), pH 7 (KH₂PO₄, NaOH), and pH 10 (KCO₃, K3BO₃, KOH) buffers immediately prior to measurement. Major elements (Na, K, Ca Si, Mg) were determined by inductively coupled plasma-optical emission spectrometry (iCAP 6000, Thermo Fisher Scientific, Waltham, MA, USA).

Following collection, dissolved metals samples were acidified with 1 M HCl prepared from trace metal grade 12 N HCl (Fisher Scientific, Pittsburgh, PA, USA) and 18 M Ω deionized water. Filters and collected particles were digested in reverse *aqua regia* (3:1 v/v HNO $_3$: HCl), dried down at 70 °C in a trace-metal free hood, and brought up in 20 ml 2% HNO $_3$ using trace metal grade reagents and 18 M Ω deionized water. Samples were diluted 100× in 2% HNO $_3$ prior to analysis.

Trace element analyses were performed at University of Minnesota using a triple quadrupole inductively coupled plasma mass spectrometer (Thermo Fisher Scientific iCAP TQ, Waltham, MA, USA) measured against matrix-matched standard lines prepared

NEPTUNE Cabled Observatory



Main Endeavour Field B Hulk Seismometer Chain 2 TP Lobo Hydrophone 2^{1/3} ABCP ABCP

Fig. 1. (A) Overview map of the NEPTUNE cabled observatory and (B) detail map of the Main Endeavour Field and associated NEPTUNE infrastructure. The vent fluid sampler was deployed at the MEF South BARS instrument node (black rectangle) located a few meters away from the historical Smoke & Mirrors (S&M) vent deposit structure. Continuous power and communications were delivered through cabled connection to junction box JB-10. Vent deposit structure names are as in Delaney et al. (1992). Labels are slightly offset to allow greater visibility of deposit structures on the background bathymetric map.

Table 1

Concentrations of trace metals and select chemical components in vent fluid samples collected from Main Endeavour Field in 1999 (Seewald et al., 2003). Chloride, volatile, and metal concentrations are endmember values extrapolated to zero-Mg (e.g., Von Damm et al., 1985); "min. Mg" is the lowest Mg sample collected from a given vent, indicative of mixture with seawater prior to or during sample acquisition. Temperature, pH and dissolved ions including metals are from Seyfried et al. (2003); Volatiles are from Seewald et al. (2003)^a. Vent locations are illustrated in Fig. 1.

Vent	Temp. ° C	pH 25°C	min. Mg mmol/kg	Cl mmol/kg	H ₂ mmol/kg	H ₂ S mmol/kg	CH ₄ mmol/l	NH3 μmol/kg
Dante Bastille	350 368	3.72 3.44	13.3 5.84	418 208	0.52 0.62	13 22	na 1.7	529 602
Cantilever	375	3.74	2.43	32	25	25	1.7	645
V		-		NT:	C	-	0.1	
Vent	Mn μmol/kg	Fe μmol/kg	Co nmol/kg	Ni nmol/kg	Cu µmol/kg	Zn μmol/kg	Cd nmol/kg	Mo nmol/kg
Dante								
	μmol/kg	μmol/kg	nmol/kg	nmol/kg	μmol/kg	μmol/kg	nmol/kg	nmol/kg

from NIST-traceable single- and multi-element standards (SPEX CertiPrep, Metuchen, NJ, USA). Because of a lack of certified reference materials for hydrothermal fluids, analytical errors were estimated by interspersed measurements of matrix-matched control samples containing similar concentrations of trace elements as measured samples. Process blanks were determined by analyses of digested blank filters. Element specific detection limits, quantification limits, blank levels, and estimated errors are detailed in Table 3.

3.3. Solubility calculations, in situ pH

Hydrothermal fluid pH and mineral saturation states were calculated using Geochemists' Workbench (Bethke and Yeakel, 2012). Thermodynamic properties at 220 bar were calculated using Py-GeoChemCalc (https://bitbucket.org/Tutolo-RTG/pygcc/src/master/), a Python version of formulas contained in DBCreate (Kong et al., 2013). Thermodynamic data for Mo species were calculated using the Unitherm module of HCh (Shvarov, 2008) based on data

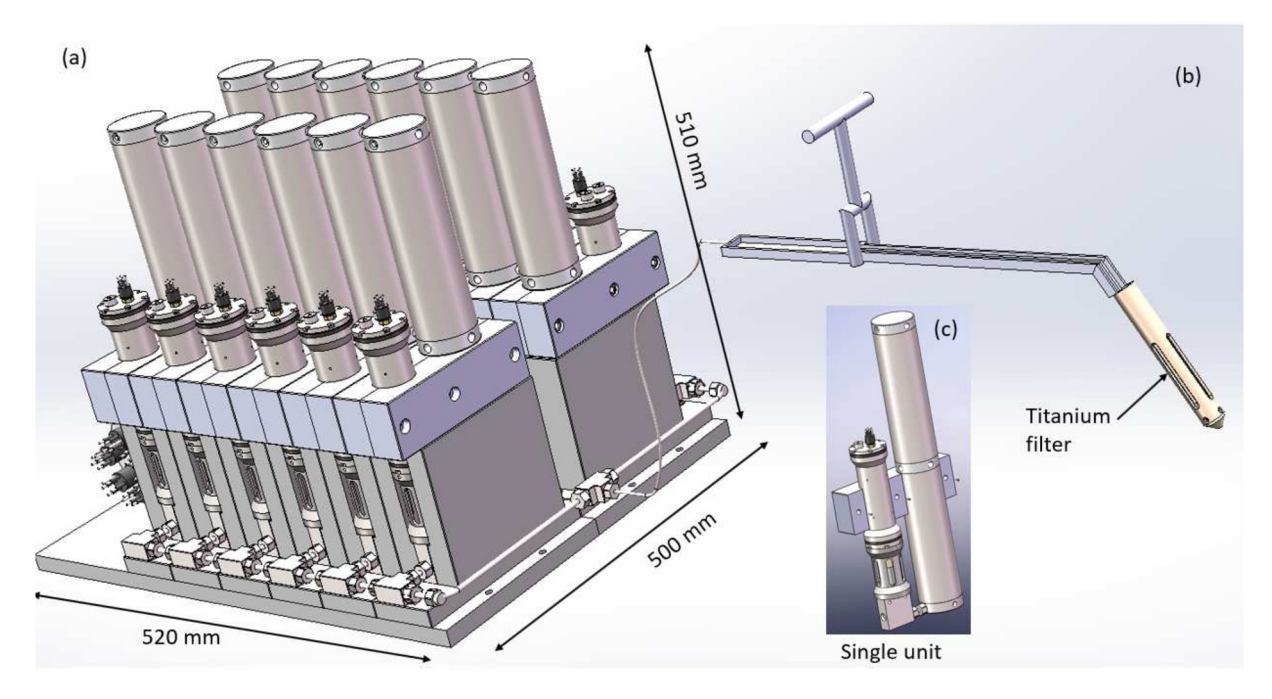


Fig. 2. Diagram of the remotely operated serial vent fluid sampler (Seyfried et al., 2022). (a) Main body comprises a computer control and a sample vessel manifold composed of 12 independently operated grade 2 titanium isobaric gastight samplers. The sampler manifold is connected to the sampling snorkel (b) by PEEK tubing.

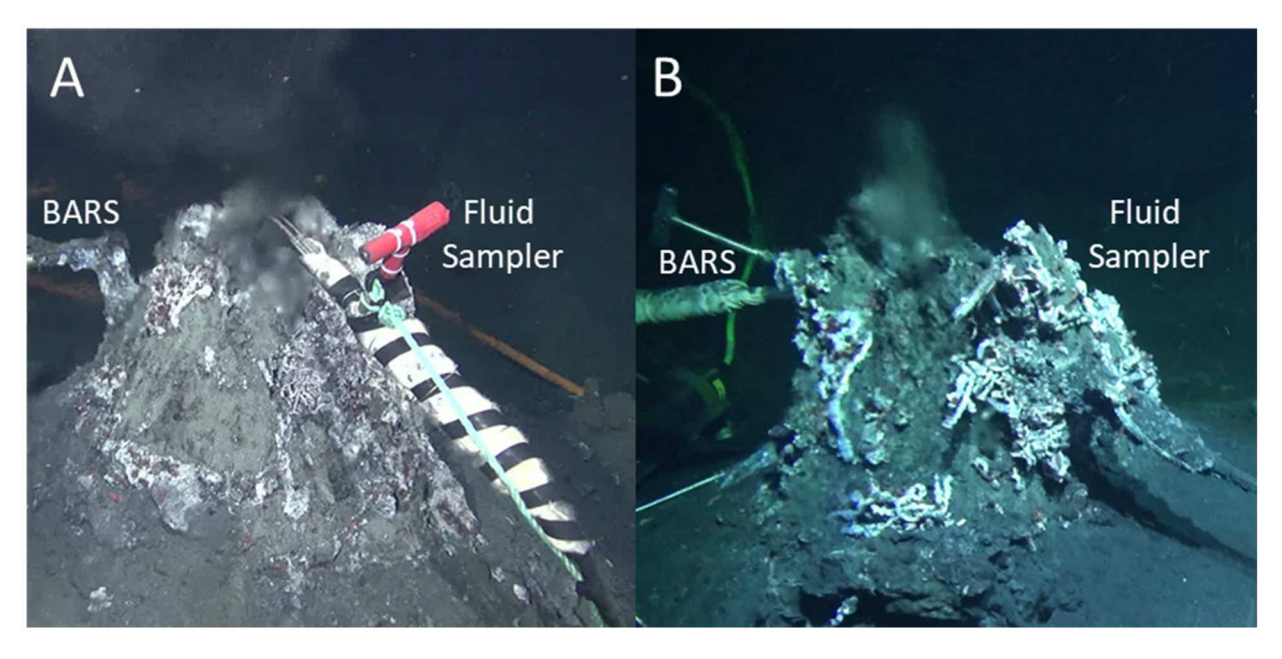


Fig. 3. Images of the vent fluid sampler (A) immediately after deployment (September 21, 2019) and (B) before recovery (June 11, 2020). Also shown is the BARS temperature/resistivity sensor located in the same chimney structure (left in both images). Mineralization of the sampler nozzle served to isolate the sampler inlet from ambient seawater. Original photographs taken by ROV *Odysseus*, obtained from Ocean Networks Canada, SeaTube V3 (https://data.oceannetworks.ca/SeaTubeV3). Heading in left image = 246°. Heading in right image = 283°.

from Robie and Hemingway (1995) for molybdenite, Shock et al. (1997) for MoO_4^{2-} , Minubayeva and Seward (2010) for HMoO_4^{-} and $\text{H}_2\text{MoO}_4(\text{aq})$, and Shang et al. (2020) for NaHMoO4. Data for Zn^{2+} and sphalerite were updated with data from Tagirov and Seward (2010) following Xing et al. (2022). Relevant input, database, and output files are included in supplementary materials.

Seafloor vent fluid chemistry was reconstructed by adding back the elemental content of the precipitate fraction to the dissolved fluid chemistry and calculating the speciation and mineral saturation states of fluid samples at seafloor conditions (220 bar, $281-304\,^{\circ}\text{C}$). Sulfide, which was not measured in precipitates, was added back to the fluid composition in equimolar ratio with Fe and

Zn, resulting in a 0.3–9.2% increase in total sulfide. Calculation of $in\ situ$ pH is based on saturation with respect to chalcopyrite or pyrite, consistent with the composition of mineralization on the fluid sampler and the previously deployed temperature-pH-redox sensor removed to install the fluid sampler (Fig. 4). Vent fluid pH values calculated for $in\ situ$ temperatures are 0.2–0.5 pH units higher than those measured at 25 °C (Table 2).

4. Results

Compared to ambient seawater, S&M 2019-2020 vent fluids are greatly depleted in Mg and sulfate (94-99.6% and 95-99.7%, re-

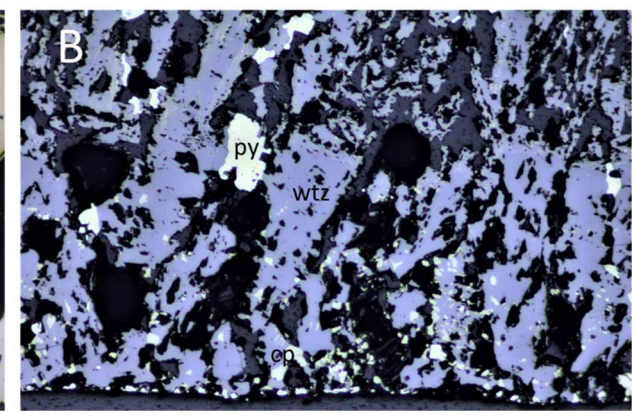


Fig. 4. Photomicrographs of: (A) mineralization collected from sensor deployed in the same vent orifice as the sampler that was removed prior to installation of the sampler; estimated fluid temperature = 300 °C; (B) mineralization collected from the sampler snorkel; estimated fluid temperature = 281 °C. Bottom edge of each sample was originally attached to a non-porous titanium sensor/sampler snorkel wall and grew in contact with vent fluid, located upward in photomicrographs. cp=chalcopyrite; wtz=wurtzite. Image width is 1.6 mm.

spectively), 14–29% depleted in Na, 3.0–3.5 \times enriched in Ca, and 2.1–2.5 \times enriched in K, consistent with high-temperature basalt-seawater reactions (e.g., Seyfried, 1987), and previous analyses of MEF vent fluids (Butterfield et al., 1994; Seyfried et al., 2003). Chloride concentrations are 18–23% depleted relative to seawater, indicative of sub-surface phase separation prior to venting. Dissolved $\rm H_2$ and $\rm H_2S$ concentrations are consistent with high-temperature reactions in the presence of a moderately reducing set of mineral buffers such as anhydrite-magnetite-pyrite (Seyfried et al., 2002).

Notably, the lowest Mg and sulfate concentrations obtained in S&M 2019–2020 vent fluids are consistent with those of high-temperature basalt-seawater and mineral-buffer experiments (Seyfried et al., 2002), suggesting little-to-no contamination of these samples by ambient seawater. While still low in comparison to typical seafloor sampling, Samples 3–6 contain higher and strongly correlated concentrations of Mg and sulfate, suggesting minor addition of seawater-like Mg- and sulfate-containing fluid. Based on systematic deviation of the Mg:sulfate from that of seawater and a lack of temperature change at the vent, Seyfried et al. (2022) propose that Mg- and sulfate addition is caused by subsurface injection of hot (>150 °C) seawater-like fluid not yet chemically equilibrated with seafloor crust.

Except for Mo, which is variably depleted and enriched relative to seawater, transition metal- and silica concentrations are highly enriched relative to seawater. Mineralization collected from the sampler snorkel contains bladed wurtzite and intergrown chalcopyrite with subhedral pyrite (Fig. 4B). Mineralization collected from the previously deployed temperature/pH/redox sensor comprises euhedral pyrite and massive chalcopyrite (Fig. 4A). Thermodynamic modeling based on measured fluid chemistry and equilibrium with respect to pyrite indicates that *in situ* pH= 4.16–4.53 and fluids are saturated or near-saturated with respect to chalcopyrite. All samples are calculated to be undersaturated with respect to sphalerite but become saturated if conductively cooled 20–30 °C. Considering model uncertainties, these results suggest that vent fluids are saturated or near saturated with respect to sphalerite and/or wurtzite.

4.1. Vent fluid temperatures and metal concentrations

Vent fluid temperatures as recorded by the BARS resistivity/temperature sensor indicate that Samples 1–6 were collected at $302-304\,^{\circ}\text{C}$ while Samples 7–9 were collected at $281-282\,^{\circ}\text{C}$ (Fig. 5A). The most abundant transition metal in Samples 1–6 is

Zn, followed by Fe and Mn. This order is reversed in Samples 7–9, where Mn>Fe>Zn (Table 2, Fig. 5). Compared to Samples 1–2 and Samples 7–9, Samples 3–6 contain elevated concentrations of Mg and sulfate (Table 1). Close analysis of these fluids by Seyfried et al. (2022) suggests that elevated Mg and sulfate concentrations are not directly the result of contamination by cold seawater, as vent fluid temperature does not noticeably change during this period and vent fluid Mg:sulfate ratios are slightly elevated above that of seawater. However, Co and Mo both decreased significantly between Samples 1–2 and Samples 3–6, indicating that this incursion of Mg- and sulfate-containing fluid does have an effect on concentrations and likely subsurface deposition rates of these metals, whether by a subtle change in fluid temperature or chemistry, e.g., a slight increase in pH.

A second, more obvious change in vent fluid temperature and composition occurred on March 13, 2020, when BARS recorded vent fluid temperatures decreased ~20 °C over ~20 hours (Fig. 5B). The BARS-mounted thermocouple exhibits minimal sensor drift, as evidenced by regular maintenance cruises and performance confirmation by ROV-mounted thermocouples over several years. However, BARS recorded vent fluid temperatures and coupling with the fluid sampler are sensitive to mineralization of the BARS temperature sensor and/or the fluid sampler. That the March 13, 2020, temperature change recorded by the BARS reflects an actual change in vent fluid temperature and not a sampling artifact caused by mineralization of the sensor is supported by concurrent decreases in temperature-sensitive metals (e.g., Cu, Zn, Mo) in associated fluid samples.

On average, Samples 1–6 contain $15\times$ as much Cd, $13\times$ as much Zn, $10\times$ as much Cu, and $5\times$ as much Mo and as Samples 7–9 (Table 3, Fig. 6K, I, H). Concentrations of Cu, Zn, and Cd are highly correlated ($R^2 > 0.98$) with an average molar Zn/Cu ratio = 23 ± 1 and Zn/Cd = 1050 ± 30 (Fig. 7A, B). Molybdenum is moderately correlated with Zn ($R^2 = 0.65$, Fig. 7C) with an average Zn/Mo ratio of 3000 ± 300 (Fig. 7C).

Iron responds only weakly to the observed temperature drop, with variability in Samples 1–6 (Fe = 281–777 μ mol/kg) exceeding differences between Samples 1–6 and Samples 7–9. Vanadium, Mn Cr, Co, and Ni do not vary in response to the observed temperature drop (Table 3, Fig. 6D, C, F, G). However, Ni, Co, Cr, and to some extent V, are elevated in Sample 1, as well as Sample 2 for Co. Concentrations of Ni and Cr are strongly correlated (R² = 0.98, Fig. 7D).

Table 2Vent fluid temperature, major element chemistry and in situ pH calculated by thermodynamic modeling. Data are from Seyfried et al. (2022). An analysis of IAPSO standard seawater (salinity = 33.992 practical salinity units) is included for comparison.

Sample	Date	Days deployed	Temp. ° C	pH, NBS at 25°C	H2 mmol/kg	H2S mmol/kg	Cl mmol/kg
1	10/8/2019	17	302	4.21	0.23	2.7	424
2	11/1/2019	41	302	4.29	0.24	3.3	443
3	11/20/2019	60	302	4.22	0.23	2.8	453
4	12/12/2019	82	302	4.49	0.22	3.6	437
5	1/15/2020	116	303	4.27	0.20	3.4	451
6	2/28/2020	160	304	4.06	0.21	3.2	432
7	3/19/2020	180	281	4.22	0.21	3.1	428
8	4/17/2020	209	282	4.37	0.24	3.5	432
9	5/26/2020	248	281	4.13	0.23	3.4	429
Seawater	IAPSO		2	7.8	_	_	559
Error			0.5	0.05	5%	10%	3%

Sample	Na mmol/kg	Ca mmol/kg	K mmol/kg	Si mmol/kg	Mg mmol/kg	Sulfate mmol/kg	pH, calc. in situ
1	330	30.9	21.5	14.1	0.24	0.12	4.43
2	349	33.1	22.8	15.2	0.19	0.09	4.68
3	400	35.3	25.1	16.4	2.55	1.05	4.47
4	337	30.1	21.0	13.3	2.35	0.71	4.85
5	368	32.3	22.7	14.7	3.07	1.4	4.71
6	350	31.9	22.0	15.1	1.39	0.63	4.26
7	347	31.5	21.5	14.8	0.8	0.21	4.43
8	349	32.4	21.2	14.8	0.63	0.23	4.58
9	332	31.8	22.7	15.4	0.56	0.23	4.38
Seawater	454	10.5	10.7	_	52.3	28.6	_
Error	3%	2%	5%	5%	5%	2%	

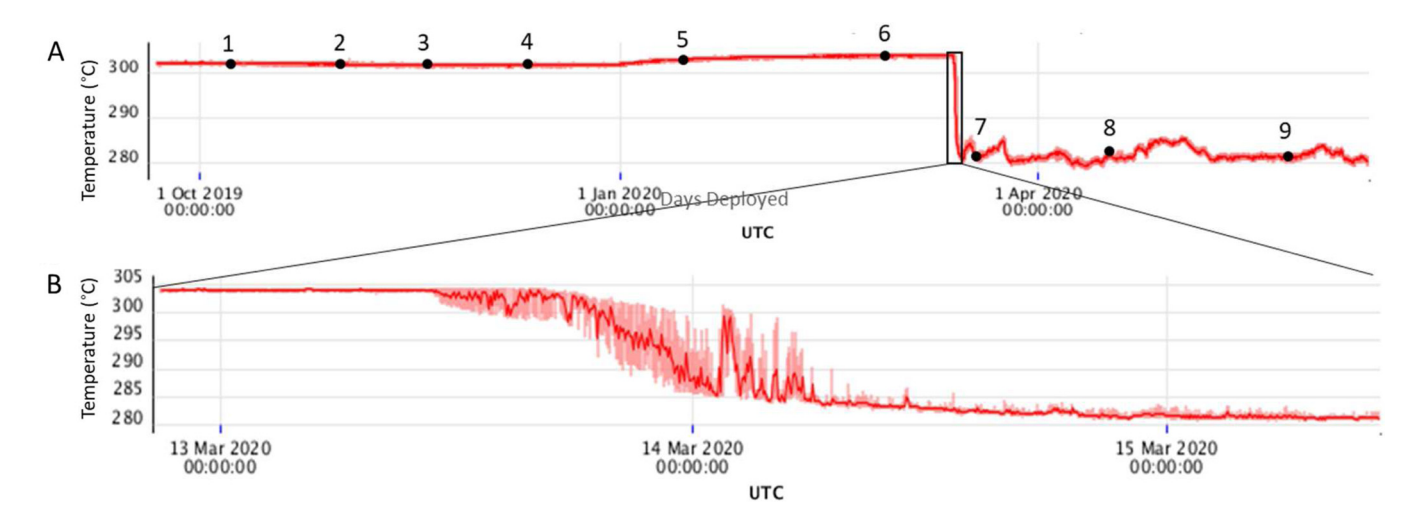


Fig. 5. Vent fluid temperature as recorded by the BARS resistivity/temperature sensor during (A) the duration of the vent fluid sampler deployment and (B) the observed temperature change. Data and original plots from Ocean Networks Canada: Plotting Utility (https://data.oceannetworks.ca/PlottingUtility). Fluid samples are marked as black circles.

4.2. Trace element partitioning

Cooling within the sample vessels leads to precipitation of metal- and sulfide-rich particles. Chemical analyses indicate that these (>0.2 μ m) particles are predominantly Zn- and Fe sulfides. Partitioning of a trace element during closed system phase separation can be modeled by the following formula (e.g., Neumann et al., 1954):

$$\frac{[T]/[M]_{solid}}{[T]/[M]_{total}} = \frac{D_{T/M}^{solid/aqueous}}{\left(D_{T/M}^{solid/aqueous} \times F_{M,solid}\right) + \left(1 - F_{M,solid}\right)}$$

where $[T]/[M]_{solid}$ is the trace-element/major-element ratio of the sampler precipitate, $[T]/[M]_{total}$ is the trace-element/major-element ratio of the whole fluid, $D_{T/M}^{solid/aqueous}$ is the partitioning coefficient of the trace element into sampler precipitates rela-

tive to the major element, and $F_{M,\ solid}$ is the mole fraction the major element incorporated into sampler particles. For simplicity, $D_{T/M}^{solid/aqueous}$ is assumed constant. This formula is most sensitive to the partition coefficient $D_{T/M}^{solid/aqueous}$, when $F_{M,\ solid}$ is small. However, the appropriateness of the closed-system equilibrium partitioning model is best evaluated if $F_{M,\ solid}$ covers a range of values 0–1

The metal fractions contained in sampler particulates range from 0–2% for Mn to 97–100% for Zn and Cd (Table 4). Iron, V, Cr, Ni, and Co, and Mo exhibit intermediate particulate fractions (Table 4). Ratios of V/Fe and Mo/Fe fit closely with a model of closed system equilibrium partitioning into Fe particles with $D_{V/Fe}$ = 24, $D_{Mo/Fe}$ = 46 (Fig. 8A, C). Ratios of Cr/Fe deviate from model projections and do not converge to a solid/total Cr/Fe ratio of 1, as expected for a simple partitioning model. This deviation from simplified model expectations could be accounted for by precip-

Table 3Nutrient transition metal concentrations in dissolved and particulate fractions and whole fluids. Analyses of a digested blank filter and seawater collected in a titanium integrated gastight sampler are listed for comparison. The two dissolved fractions for Sample 1 are replicate dilutions indicative of combined laboratory and analytical precision.

	V nmol/kg	Cr umol/kg	Mn umol/kg	Fe umol/kg	Co nmol/kg	Ni nmol/kg	Cu umol/kg	Zn umol/kg	Mo nmol/kg	Cd nmol/kg	W nmol/kg
Detection Limit Quantification Limit	1 3	0.054 0.18	0.0 0.04	0.4 1.30	2 8	14 47	0.02 0.08	0.01 0.05	1.3 4.3	1 3	0.5 1.6
Estimated Error	17%	15%	2%	2%	3%	1%	10%	4%	6%	7%	5%
Blank Filter ^a Seawater ^b	5 36.5	0.12 bdl	0.04 0.05	1.91 3.3	3 1.4	35 42	0.05 0.13	0.19 0.6	15.1 107	2 0.8	8.3 5.2
Sample 1 Dissolved Dissolved ^c	104 105	0.37 0.40	215 219	171 174	4 3	361 259	0.4 1.9	3.3 11.7	20 20	5 8	5.0 4.8
Dregs Total	409 513	5.06 5.45	0.8 218	108 281	15 18	1008 1318	16.5 17.7	436 443	199 220	433 439	11.9 16.7
Sample 2 Dissolved Dregs	93 198	0.26 0.94	237 1.4	180 205	3 15	127 201	0.4 26.0	10.8 699	8 192	10 687	5.4 4.1
Total Sample 3	291	1.20	238	385	18	329	26.4	710	200	697	9.5
Dissolved Dregs Total	130 280 410	0.64 0.70 1.34	218 3.1 221	161 280 441	4.8 3.0 7.8	182 180 362	0.1 17.4 17.4	2.5 447 450	6 126 132	2 444 446	10.9 4.3 15.2
Sample 4 Dissolved Dregs	105 113	0.30 0.15	209 0.8	156 128	4.6 1.9	204 91	0.1 11.6	0.8 336	10 89	1 308	32.9 5.0
Total Sample 5 Dissolved	218 97	0.45 0.26	210 215	284 148	6.6 4.8	294 128	11.7 0.1	337 1.5	100 5	309 1	37.9 11.1
Dregs Total	324 422	0.17 0.43	3.9 219	629 777	1.3 6.1	57 186	33.0 33.0	740 742	117 122	849 850	4.9 16.0
Sample 6 Dissolved Dregs	105 228	0.22 0.35	221 1.8	147 240	2.2 1.8	114 111	0.1 11.5	0.6 258	2 56	0 281	2.3 1.2
Total Sample 7	333	0.57	223	387	4.0	225	11.6	259	58	282	3.5
Dissolved Dregs Total	87 240 326	0.37 0.19 0.56	218 0.3 219	158 30 189	3.2 1.1 4.3	271 74 345	0.1 1.5 1.6	1.0 34.9 35.9	3 27 30	1 27 28	3.1 0.9 4.0
Sample 8 Dissolved Dregs	53 318	0.25 0.13	224 0.5	161 53	2.5 0.7	124 48	0.04 2.6	0.6 53.7	4 25	0 56	5.0 0.8
Total Sample 9	370	0.38	225	214	3.2	171	2.6	54.4	29	56	5.8
Dissolved Dregs Total	95 270 365	0.28 0.22 0.50	219 1.0 220	151 25 176	6.0 0.9 6.9	160 37 197	0.04 1.4 1.4	0.5 21.0 21.5	2 27 29	0 16 16	5.3 5.5 10.8

^a Analysis of blank filter digested in reverse aqua regia, reported to equivalent dilution factor as dregs samples.

itation of Cr-enriched (e.g., oxide) and Cr-depleted (e.g., sulfide), Fe-rich particles. However, because priority was given to quantitative analysis of fluid samples, the exact mineralogy of sampler precipitates is unknown. Ratios of Co/Fe and Ni/Fe closely reflect those of the total fluid, suggesting partitioning coefficients, $D_{\text{Co/Fe}} \approx 1$ and $D_{\text{Ni/Fe}} \approx 1$, during Fe mineral precipitation within the samplers.

5. Discussion

Elemental analyses of vent fluids collected as part of the S&M 2019–2020 time series reveal coherent patterns –consistent major elements and correlations among temperature-sensitive trace elements– suggesting that differences in measured sample compositions reflect real changes in vent fluid chemistry rather than sampling artifacts. Except for Mn, large and variable fractions of

Table 4 Element Particulate Fraction.

	Minimum	Maximum
V	52%	86%
Cr	33%	93%
Mn	0%	2%
Fe	14%	81%
Co	13%	85%
Ni	19%	76%
Cu	93%	100%
Zn	97%	100%
Mo	86%	96%
Cd	97%	100%

nutrient transition metals are incorporated into sampler precipitates (Table 4; similar tables in Trefry et al., 1994; Schmidt et al.,

^b Analysis of seawater collected with Integrated Gastight Sampler.

c Replicate analysis; Fluid total based on average of two replicates. bdl = below detection limit.

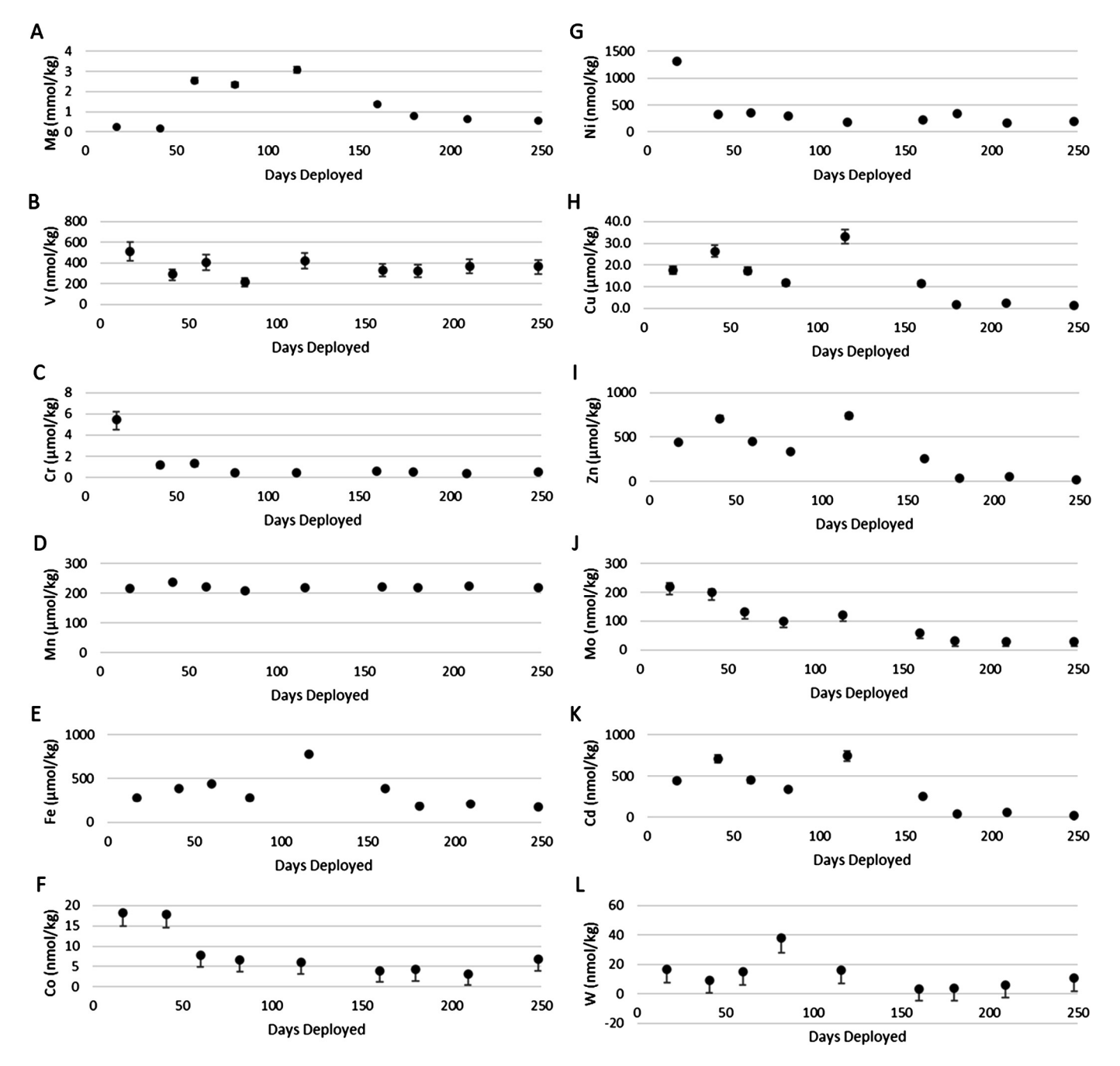


Fig. 6. Nutrient Transition Metal Concentrations in S&M 2019–2020 Fluids, X-axis is the number of days since sampler deployment. Positive error bars represent 1σ estimated errors; negative error bars include possible laboratory contamination based on blank filter analysis (Table 3).

2007). Thus, meaningful data on most transition metal nutrients can only be obtained if sampler precipitate fractions are quantitatively collected and analyzed. Importantly, the S&M 2019–2020 time series samples contain very low concentrations of Mg and sulfate, indicative of little-to-no contamination by ambient seawater, providing unprecedented insight into hydrothermal vent fluid compositions and related processes.

Cabled connection of the sampler to the NEPTUNE observatory led to several unforeseen advantages. First, the extended deployment period allowed time for the vent deposit to grow around the snorkel head, effectively isolating it from ambient seawater. Second, collection of many samples from a single location over a period of several months allows the combined consistency of repeat sampling and vent fluid chemistry to be effectively evalu-

ated. Third, connection to the NEPTUNE observatory allowed for continuous co-located temperature monitoring. This third point proved essential as strictly co-located temperature monitoring provided by the thermocouple inherent to the fluid sampler was lost when the reference thermocouple failed prior to the first fluid sampling. However, continuous proximal temperature monitoring was provided by a "BARS" resistivity/temperature probe (Larson et al., 2007) installed in the same chimney structure throughout the duration of the deployment (Fig. 3). Comparative temperature readings of fluids venting from both orifices obtained during installation and removal of sampling devices and during the period in which the fluid sampler thermocouple was working strongly suggest that these two devices are effectively co-located with respect to fluid temperature.

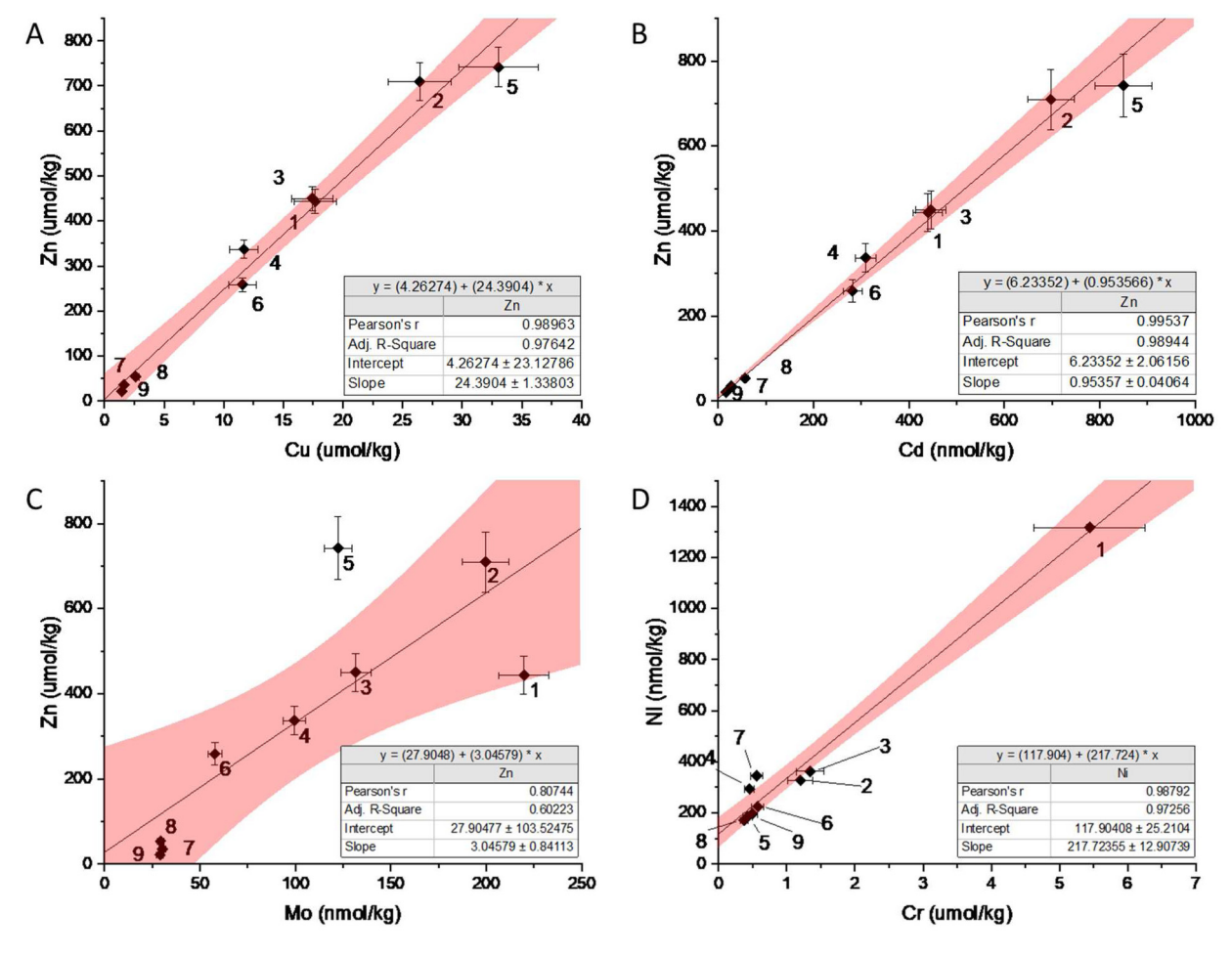


Fig. 7. Concentrations of Zn vs. Cu, Cd, and Mo and Cr vs. Ni.

5.1. Response to temperature change

On March 13, 2020, vent fluid temperatures decreased from 304 °C to 281–282 °C over \sim 20 hours (Fig. 5B). In the absence of fluid chemistry, this decrease would likely be attributed to entrainment of cold seawater and/or a localized change in fluid flow around the BARS resistivity/temperature sensor. However, low Mg and sulfate concentrations and decreased metal concentrations support a real change in vent fluid temperature without significant inmixing of ambient seawater. The \sim 20 hour duration of this temperature drop in the context of months-long stability in vent fluid temperature is consistent with seismically induced changes in near-surface fluid flow. Previous field observations (e.g., Fornari et al., 1998; Sohn et al., 1998; Johnson et al., 2000; Hooft et al., 2010) and model calculations (Wilcock, 2004; Ramondenc et al., 2008) suggest that seismically induced temperature changes can occur within days of a seismic event, reflecting changes in subseafloor permeability. Further analyses of contemporaneous seismic data collected by the NEPTUNE observatory may provide greater insight into the causes of the observed temperature decrease and related changes in vent fluid chemistry.

Concentrations of Cu, Zn, Cd, and to a lesser extent Mo and Fe respond strongly to the observed $\sim\!20\,^{\circ}\text{C}$ temperature drop. Solubility calculations and mineral samples obtained from sampling devices installed in the vent orifice indicate S&M 2019–2020 vent fluids are saturated with respect to chalcopyrite and pyrite, and likely saturated or nearly saturated with respect to wurtzite. Concentrations of Cu and Zn are somewhat higher than those previously reported for MEF vent fluids (Seyfried et al., 2003) and other luan de Fuca vent fields (Trefry et al., 1994), and may indicate

slight localized enrichment attributable to ongoing dissolution of near-surface sulfide deposits and/or less complete recovery of insoluble elements in previous samples.

The observed Zn/Cd molar ratio of 1050 ± 30 is consistent with subsurface remobilization of Cd-containing zinc sulfides, as supported by previously reported Zn/Cd in hydrothermal fluids (Zn/Cd = 600-1200; Metz and Trefry, 2000), and exhalative zinc deposits (Zn/Cd = 575-1150; Schwartz, 2000). In contrast, the observed Zn/Cu ratio of 23 ± 1 is not consistent with congruent dissolution of Zn-containing chalcopyrite or Cu-containing sphalerite. Experimental studies indicate chalcopyrite can maximally accommodate 0.9 mol% Zn and sphalerite can maximally accommodate 2.4 mol% Cu (Kojima and Sugaki, 1985). The observed Zn/Cu ratio could indicate congruent dissolution/precipitation of a chemically and mineralogically homogeneous subsurface deposit, in which case vent fluid Zn/Cu ratios would reflect the bulk composition of underlying deposits.

More generally, these combined temperature and vent chemistry data indicate an oscillating dynamic of subsurface deposits and venting fluids in response to changes in vent fluid temperature, most likely caused by seismically induced changes in subsurface permeability. Vent fluid cooling leads to lower fluxes of Cu, Zn, and Cd to the water column and, correspondingly, greater trapping efficiency by subsurface deposits. Conversely, heating of the system leads to redissolution of these deposits and higher vent fluid metal concentrations. Over the course of our sample collection, a $\sim 20\,^{\circ}$ C drop in temperature led to a roughly 90% decrease in vent fluid Cu, Zn, and Cd concentrations, demonstrating that even minor changes

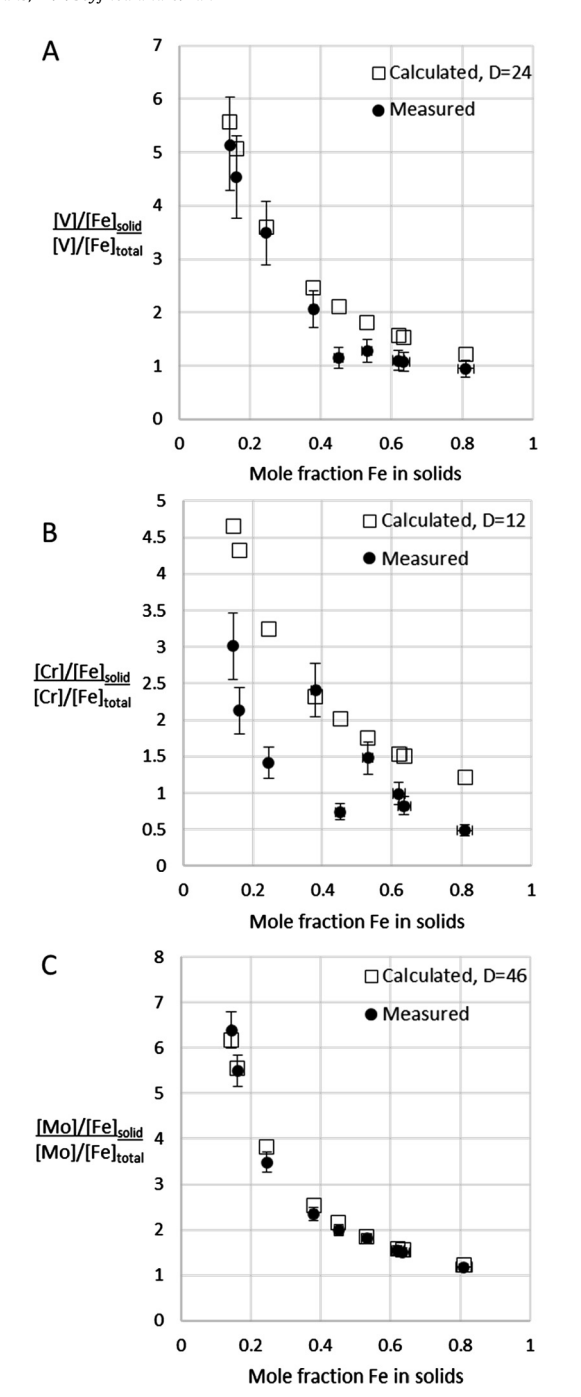


Fig. 8. Measured ratios and best-fit partitioning models of V, Cr, and Mo trace element partitioning as a substitute for Fe in sampler precipitates.

in fluid temperature can have large effects on vent fluid metal concentrations, water column inputs, and subsurface mineralization.

Separately from the March 13, 2020, drop in vent fluid temperature, Mo concentrations in Samples 3–6 are systematically lower than those in Samples 1–2 (Fig. 6J). Because Mo solubility is highly sensitive to temperature and Mo is highly supersaturated in venting fluids, this decrease may reflect a slight cooling in the system subsurface coincident with the injection of hot (>150 °C) partially reacted seawater proposed by Seyfried et al. (2022). While insufficient to noticeably affect vent fluid exit temperatures, subsurface injection of a somewhat cooler, chemically distinct fluid may be sufficient to induce subsurface precipitation of Mo and reduce Mo concentrations in venting fluids. This same process would also explain the observed decrease in Co. As can be inferred from numer-

ous ore deposit studies and, more recently, trace element analyses of drill cores from the TAG hydrothermal mound, Co and Mo are enriched in pyrite recovered from the highest-temperature sections of sulfide deposition (Grant et al., 2018).

5.2. Substrate composition

Considering the consistency in major element- and dissolved gas chemistry (Table 2), the timing of the event, and the response of elements like Cu, Zn, and Cd known to be concentrated in seafloor massive sulfide deposits, the observed $\sim\!20\,^{\circ}\text{C}$ temperature drop most likely reflects near-surface changes in vent field hydrology. Conversely, concentrations of elements that do not respond to the observed temperature drop likely reflect higher-temperature reactions between fluids and hydrothermally altered host rocks.

Seafloor rocks dredged from the Endeavour Segment comprise enriched- and transitional mid-ocean ridge basalts that exhibit ubiquitous, small-scale geochemical and mineralogical heterogeneity (Karsten et al., 1990). Concentrations of Mn, V, and W do not vary significantly in S&M 2019-2020 vent fluids, indicating that factors controlling the concentrations of these elements remain more-or-less constant throughout the sampling period. This is consistent with analyses of seafloor rocks, which indicate limited ranges in concentrations of these elements (Karsten et al., 1990). Vent fluid V and W concentrations are rarely reported, but these data suggest that V and W may behave similarly to Mn in seafloor hydrothermal systems, albeit at much lower concentrations, consistent with source rock and general solubility constraints. Concentrations of W in vent fluids from the ultramafic hosted Niebelungen vent field (W = 12-14 nmol/kg; Schmidt et al., 2011) are broadly similar to those reported here (W = 4-38 nmol/kg), suggesting little distinct contrast between basalt-hosted and ultramafic-hosted systems.

The strong correlation between Cr and Ni in S&M 2019–2020 vent fluids, lack of response to changes in vent fluid temperature, and enrichment in Sample 1 suggest these elements reflect some of the compositional heterogeneity observed in seafloor rocks. A likely source of Ni and Cr is olivine cumulates present in some Endeavour Segment basalts (Karsten et al., 1990). Olivine has also been found to preferentially react in basalt-seawater hydrothermal experiments (Berndt et al., 1989) and could be expected to release Cr and Ni. Consistent with this hypothesis, elevated concentrations of Ni have been reported in vent fluids from the ultramafic-hosted Rainbow vent field (Diehl and Bach, 2020). An interesting implication of this observation is that vent fluids may react with temporally varying localized sections of the seabed such that spatial heterogeneity in seafloor rocks may lead to subtle variations in vent fluid chemistry over time.

5.3. Molybdenum

Biologically, Mo is a functional component of methanogenesis and nitrogen fixation pathways (Joerger et al., 1988; Stiefel et al., 1993; Leigh, 2000). In some organisms, methanogenesis can be performed using W (Jones and Stadtman, 1977; Kletzin and Adams, 1996); in others, nitrogen fixation can be performed using reduced Fe or V (Bishop and Joerger, 1990; Raymond et al., 2004; Sippel and Einsle, 2017). However, genetic studies suggest that Mo-utilizing enzymes evolved before widespread oxidation of the Earth (Boyd et al., 2011) and may even have been present in the last universal common ancestor (Weiss et al., 2016). Paradoxically, geologic and geochemical studies indicate that Mo concentrations in anoxic Archean oceans were much lower than modern values (Scott et al., 2008; Saito et al., 2003; Roué et al., 2021) and continental weathering inputs were much reduced (Wille et al., 2013;

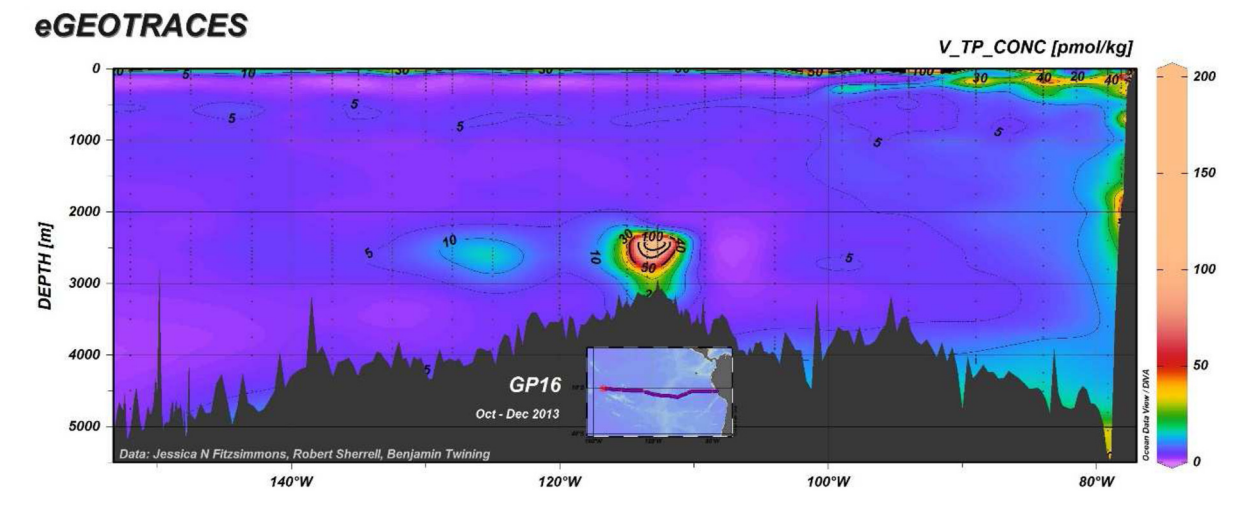


Fig. 9. Contoured profile of particulate V concentrations per kilogram seawater in a transect across the equatorial Pacific Ocean. A distinct hydrothermal plume is evident above and downcurrent of the East Pacific Rise. If background concentrations were lower, as is expected for anoxic Archean oceans, a similar profile might be derived for Mo. Figure is obtained from the eGEOTRACES website (www.egeotrace.org) (GEOTRACES, 2021). Original data are from Ho et al. (2018), which includes data on particulate Mo, not yet available through the eGEOTRACES website.

Johnson et al., 2019). Hence, Mo may have been a limiting nutrient in anoxic Archean environments with implications for nitrogen fixation and overall biological productivity (Anbar and Knoll, 2002; Anbar, 2008).

Concentrations of Mo in S&M 2019–2020 fluids are 29–220 nmol/kg, a range that spans modern seawater values (Mo = 108 \pm 3 nmol/kg; Ho et al., 2018). That elevated Mo concentrations are observed even among modest temperature (302–304 °C) vents stands in stark contrast to previous reports, wherein seafloor hydrothermal fluids are typically Mo-depleted with respect to modern seawater (Trefry et al., 1994; Metz and Trefry, 2000; Miller et al., 2011; Schmidt et al., 2011). The only previously known exception is a 363 °C vent fluid collected from the Trans-Atlantic Geotraverse (TAG) hydrothermal field (Mo = 148 nmol/kg; Metz and Trefry, 2000).

An explanation for high Mo concentrations observed here compared to the depleted values reported elsewhere is incorporation of Mo into early-formed (copper)-iron-sulfide particles, as previously proposed in a study of plume particles by Findlay et al. (2015), which are then preferentially excluded from typical vent fluid samples. Alternatively, Mo might be sourced from underlying mineral deposits. However, Mo is not enriched in other seafloor vent fluids where extensive deposit remobilization has been clearly identified (Craddock, 2009). Moreover, S&M 2019–2020 fluids are greatly oversaturated with respect to molybdenite and would not be expected to dissolve Mo even at slightly elevated subsurface temperatures.

In contrast, Mo is readily adsorbed onto iron-sulfide particles (Helz et al., 1996, 2004), especially in the presence of thiomolybdate and polysulfide species (Erickson and Helz, 2000; Vorlicek et al., 2004). Thermodynamic calculations indicate that these species are dominant in the intermediate temperature, pH, and redox conditions associated with hydrothermal fluid-seawater mixing, but not in the high temperature, low pH, reducing conditions imposed by unmixed hydrothermal fluids (Liu et al., 2020). Because the sampler used in this study was encased in the mineral structure, samples were protected from mixing and precipitation/adsorption effects that would otherwise be expected to remove Mo. Therefore, values reported here may in fact be typical of seafloor vent fluids, which suggests that hydrothermal Mo inputs are significantly higher than previously estimated (Miller et al., 2011). Analogously high reactivity has been observed for Ba, for which accurate measurements of hydrothermal fluid concentrations can only be

achieved using specialized isotopic techniques (Hsieh et al., 2021) or alternatively, by obtaining uncontaminated samples (Seyfried et al., 2022).

The incorporation of Mo into rapidly forming iron-sulfide particles also has implications for long-range transport. Molybdenum and V are preferentially partitioned into sampler particles and are presumably also incorporated into hydrothermal plume particles. Indeed, such behavior has been recognized for particulate V (Ho et al., 2018). Dynamic exchanges between particulate and dissolved phases of hydrothermal plumes, and the presence of complexing ligands, can enhance long-range transport (e.g., Sander and Koschinsky, 2011), as observed for Fe in the equatorial Pacific Ocean (Fitzsimmons et al., 2017). While relatively unimportant in the context of a modern Mo-rich ocean, such a mechanism could be significant for Mo delivery to an ancient Mo-poor ocean, with ancient ocean profiles perhaps resembling modern profiles of V (Fig. 9). In support of a plume transport mechanism for Mo, laboratory studies have shown that rapidly formed iron-sulfide particles will initially adsorb, but then release Mo as they subsequently mature and recrystallize (Helz et al., 2004). The availability of Mo-complexing ligands during this process is also likely to play a significant role in determining long-range transport potential. Analyses of Mo isotopes in modern hydrothermal fluids and plume particles could help distinguish Mo sources to these plumes and provide insight into the potential for long-range oceanic transport via hydrothermal plumes.

6. Conclusions

Advances in the design and development of vent fluid sampling systems in response to power available from seafloor cabled observatories have resulted in fundamentally new perspectives on the temporal evolution of deep-sea hydrothermal fluids and possible underlying controls. Remote acquisition of time series data over relatively long intervals from a single vent provides previously unavailable insight on the nature and effect of changes in deep seated and near surface processes that characterize such systems. These changes influence mineral dissolution and precipitation on a range of temporal and special scales and stand in stark contrast to more stable hydrothermal processes previously inferred. Moreover, use of a novel remotely operated fluid sampler enables repeat sampling of vent fluids uncontaminated by ambient seawater, and thus, provides added value to and confidence in interpretations of

the time series data. Here, we focus on nutrient transition metals (V, Cr, Co, Ni, Fe, Cu, Zn, Mo, Cd, W) in hydrothermal fluid samples from the S&M vent area of Main Endeavour Field. Despite their biological importance and potential relevance for modern and ancient ecosystems, many of these elements are rarely measured in seafloor hydrothermal fluids.

Concentrations of nutrient transition metals in hydrothermal vent fluids are typically greater than seawater, indicating a net source to the ocean. Fluids are saturated or near-saturated with respect to chalcopyrite, pyrite, and sphalerite and dramatic decreases in Cu, Zn, and Cd concentrations following a drop in vent fluid temperature from 302–304°C to 281–282°C can be attributed to interactions between hydrothermal fluids and subsurface mineral deposits at near-venting conditions, presumably in the shallow subsurface. Less dramatic decreases in Fe are also observed. In contrast, concentrations of V, Cr, Co, Ni, and W do not respond to this temperature change, suggesting these elements reflect more deep-seated higher-temperature conditions. For example, correlated Cr and Ni concentrations may represent transient interactions with subsurface basalt of variably mafic composition and cumulate olivine content.

Concentrations of Mo in these relatively moderate-temperature vent fluids are surprisingly high when compared to previous measurements of Mo in seafloor hydrothermal fluids and thermodynamic expectations based on molybdenite solubility at venting conditions. It is proposed that seafloor vent fluids likely deliver much more Mo to the ocean than previously estimated, but that much of this Mo might be rapidly adsorbed onto metal-sulfide particles formed near the vent orifice. The identification of a hydrothermal source of Mo and other nutrient transition metals is significant in light of speculation about hydrothermal delivery of nutrient transition metals to the anoxic early-Earth environments which characterize the origin and early evolution of life on Earth. Further attention and investigation of these metals should be conducted to determine more precisely the processes by which seafloor hydrothermal systems contribute to delivery and transport of these metals to the ocean.

CRediT authorship contribution statement

All authors contributed equally to the success of this manuscript.

Declaration of competing interest

The authors declare that they have no known competing financial interests or personal relationships that could have appeared to influence the work reported in this paper.

Data availability

Data will be made available on request.

Acknowledgements

The authors wish to thank the captain and crew of CCGS John P. Tully and pilots of ROV Odysseus for their efforts during deployment and recovery of the sampler and Ocean Networks Canada for building and maintaining the cabled observatory that facilitated this research. Funding for this project was provided by the U.S. National Science Foundation (EAR 1515377 and OCE 1736679) (WES) and the Metal Utilization and Selection across Eons (MUSE) Interdisciplinary Consortium for Astrobiology Research (ICAR) at the University of Wisconsin - Madison, sponsored by the National Aeronautics and Space Administration (NASA) Science Mission Directorate (19-ICAR19_2-0007), NASA Astrobiology ICAR grant [80NSSC21K0592] Title: "What life wants: Exploring the

natural selection of elements" to Betül Kaçar (PI), WES (Co-I) and GNE. We thank Drew Syverson and an anonymous reviewer for their insightful comments.

Appendix A. Supplementary material

Supplementary material related to this article can be found online at https://doi.org/10.1016/j.epsl.2022.117943.

References

- Alt, J.C., 1995. Subseafloor processes in mid-ocean ridge hydrothermal systems. In: Humphris, S., et al. (Eds.), Seafloor Hydrothermal Systems: Physical, Chemical, and Biological Interactions. In: Geophysical Monograph Series, vol. 91. AGU, Washington, D.C., pp. 85–114.
- Anbar, A.D., 2008. Elements and evolution. Science, 1481–1483.
- Anbar, A.D., Knoll, A.H., 2002. Proterozoic ocean chemistry and evolution: a bioinorganic bridge? Science 297 (5584), 1137–1142.
- Ardyna, M., Lacour, L., Sergi, S., d'Ovidio, F., Sallée, J.B., Rembauville, M., Blain, S., Tagliabue, A., Schlitzer, R., Jeandel, C., Arrigo, K.R., Claustre, H., 2019. Hydrothermal vents trigger massive phytoplankton blooms in the Southern Ocean. Nat. Commun. 10 (1), 1–8.
- Berndt, M.E., Seyfried Jr, W.E., Janecky, D.R., 1989. Plagioclase and epidote buffering of cation ratios in mid-ocean ridge hydrothermal fluids: experimental results in and near the supercritical region. Geochim. Cosmochim. Acta 53 (9), 2283–2300.
- Bethke, C.M., Yeakel, S., 2012. The Geochemist's Workbench Release 9.0 Reaction Modeling Guide. Aqueous Solutions. LLC.
- Bishop, P.E., Joerger, R.D., 1990. Genetics and molecular biology of alternative nitrogen fixation systems. Annu. Rev. Plant Biol. 41 (1), 109–125.
- Boyd, E.S., Anbar, A.D., Miller, S., Hamilton, T.L., Lavin, M., Peters, J.W., 2011. A late methanogen origin for molybdenum-dependent nitrogenase. Geobiology 9 (3), 221–232.
- Butterfield, D.A., McDuff, R.E., Mottl, M.J., Lilley, M.D., Lupton, J.E., Massoth, G.J., 1994. Gradients in the composition of hydrothermal fluids from the Endeavour segment vent field: phase separation and brine loss. J. Geophys. Res., Solid Earth 99 (B5), 9561–9583.
- Craddock, P.R., 2009. Geochemical tracers of processes affecting the formation of seafloor hydrothermal fluids and deposits in the Manus back-arc basin. Ph.D. Thesis, MIT/WHOI Joint Program in Oceanography.
- Da Silva, J.F., Williams, R.J.P., 2001. The Biological Chemistry of the Elements: the Inorganic Chemistry of Life. Oxford University Press.
- Delaney, J.R., Robigou, V., McDuff, R.E., Tivey, M.K., 1992. Geology of a vigorous hydrothermal system on the Endeavour Segment, Juan de Fuca Ridge. J. Geophys. Res., Solid Earth 97 (B13), 19663–19682.
- Diehl, A., Bach, W., 2020. MARHYS (MARine HYdrothermal Solutions) database: a global compilation of marine hydrothermal vent, fluid, end member, and seawater compositions. Geochem. Geophys. Geosyst. 21 (12). https://doi.org/10.1029/ 2020GC009385.
- Ding, K., Seyfried, W.E., 2007. In situ measurement of pH and dissolved H2 in midocean ridge hydrothermal fluids at elevated temperatures and pressures. Chem. Rev. 107 (2), 601–622.
- Erickson, B.E., Helz, G.R., 2000. Molybdenum (VI) speciation in sulfidic waters: stability and lability of thiomolybdates. Geochim. Cosmochim. Acta 64 (7), 1149–1158.
- Evans, G.N., Tivey, M.K., Monteleone, B., Shimizu, N., Seewald, J.S., Rouxel, O.J., 2020. Trace element proxies of seafloor hydrothermal fluids based on secondary ion mass spectrometry (SIMS) of black smoker chimney linings. Geochim. Cosmochim. Acta 269, 346–375.
- Findlay, A.J., Gartman, A., Shaw, T.J., Luther III, G.W., 2015. Trace metal concentration and partitioning in the first 1.5 m of hydrothermal vent plumes along the Mid-Atlantic Ridge: TAG, Snakepit, and Rainbow. Chem. Geol. 412, 117–131.
- Fitzsimmons, J.N., Boyle, E.A., Jenkins, W.J., 2014. Distal transport of dissolved hydrothermal iron in the deep South Pacific Ocean. Proc. Natl. Acad. Sci. 111 (47), 16654–16661.
- Fitzsimmons, J.N., John, S.G., Marsay, C.M., Hoffman, C.L., Nicholas, S.L., Toner, B.M., German, C.R., Sherrell, R.M., 2017. Iron persistence in a distal hydrothermal plume supported by dissolved-particulate exchange. Nat. Geosci. 10 (3), 195–201.
- Fornari, D.J., Shank, T., Von Damm, K.L., Gregg, T.K.P., Lilley, M., Levai, G., Bray, A., Haymon, R.M., Perfit, M.R., Lutz, R., 1998. Time-series temperature measurements at high-temperature hydrothermal vents, East Pacific Rise 9 49′–51′ N: evidence for monitoring a crustal cracking event. Earth Planet. Sci. Lett. 160 (3–4), 419–431.
- Gartman, A., Findlay, A.J., 2020. Impacts of hydrothermal plume processes on oceanic metal cycles and transport. Nat. Geosci. 13 (6), 396–402.
- GEOTRACES Intermediate Data Product Group, 2021. The GEOTRACES Intermediate Data Product 2021 (IDP2021). NERC EDS British Oceanographic Data Centre NOC. https://doi.org/10.5285/cf2d9ba9-d51d-3b7c-e053-8486abc0f5fd.

- German, C.R., Seyfried, W.E., 2014. 8.7-hydrothermal processes. In: Holland, H.D., Turekian, K.K. (Eds.), Treatise on Geochemistry, 2nd edn. Elsevier, Oxford, pp. 191–233.
- German, C.R., Campbell, A.C., Edmond, J.M., 1991. Hydrothermal scavenging at the Mid-Atlantic Ridge: modification of trace element dissolved fluxes. Earth Planet. Sci. Lett. 107 (1), 101–114.
- Grant, H.L., Hannington, M.D., Petersen, S., Frische, M., Fuchs, S.H., 2018. Constraints on the behavior of trace elements in the actively-forming TAG deposit, Mid-Atlantic Ridge, based on LA-ICP-MS analyses of pyrite. Chem. Geol. 498, 45–71.
- Helz, G.R., Miller, C.V., Charnock, J.M., Mosselmans, J.F.W., Pattrick, R.A.D., Garner, C.D., Vaughan, D.J., 1996. Mechanism of molybdenum removal from the sea and its concentration in black shales: EXAFS evidence. Geochim. Cosmochim. Acta 60 (19), 3631–3642.
- Helz, G.R., Vorlicek, T.P., Kahn, M.D., 2004. Molybdenum scavenging by iron monosulfide. Environ. Sci. Technol. 38 (16), 4263–4268.
- Ho, P., Lee, J.M., Heller, M.I., Lam, P.J., Shiller, A.M., 2018. The distribution of dissolved and particular Mo and V along the U.S. GEOTRACES Eact Pacific Zonal Transect (GP16): the roles of oxides and biogenic particles in their distributions in the oxygen deficient zone and the hydrothermal plume. Mar. Chem. 201, 242–255. https://doi.org/10.1016/j.marchem.2017.12.003.
- Hooft, E.E., Patel, H., Wilcock, W., Becker, K., Butterfield, D., Davis, E., Dziak, R., Inderbitzen, K., Lilley, M., McGill, P., Toomey, D., Stakes, D., 2010. A seismic swarm and regional hydrothermal and hydrologic perturbations: the northern Endeavour segment, February 2005. Geochem. Geophys. Geosyst. 11 (12).
- Hsieh, Y.T., Bridgestock, L., Scheuermann, P.P., Seyfried, W.E., Henderson, G.M., 2021. Barium isotopes in mid-ocean ridge hydrothermal vent fluids: a source of isotopically heavy Ba to the ocean. Geochim. Cosmochim. Acta 292, 348–363.
- Joerger, R.D., Bishop, P.E., Evans, H.J., 1988. Bacterial alternative nitrogen fixation systems. CRC Crit. Rev. Microbiol. 16 (1), 1–14.
- Johnson, H.P., Hutnak, M., Dziak, R.P., Fox, C.G., Urcuyo, I., Cowen, J.P., Nabelek, J., Fisher, C., 2000. Earthquake-induced changes in a hydrothermal system on the Juan de Fuca mid-ocean ridge. Nature 407 (6801), 174–177.
- Johnson, A.C., Romaniello, S.J., Reinhard, C.T., Gregory, D.D., Garcia-Robledo, E., Revsbech, N.P., Canfield, D.E., Lyons, T.W., Anbar, A.D., 2019. Experimental determination of pyrite and molybdenite oxidation kinetics at nanomolar oxygen concentrations. Geochim. Cosmochim. Acta 249, 160–172.
- Jones, J.B., Stadtman, T.C., 1977. Methanococcus vannielii: culture and effects of selenium and tungsten on growth. J. Bacteriol. 130 (3), 1404–1406.
- Karsten, J.L., Delaney, J.R., Rhodes, J.M., Liias, R.A., 1990. Spatial and temporal evolution of magmatic systems beneath the Endeavour Segment, Juan de Fuca Ridge: tectonic and petrologic constraints. J. Geophys. Res., Solid Earth 95 (B12), 19235–19256.
- Kleint, C., Zitoun, R., Neuholz, R., Walter, M., Schnetger, B., Klose, L., Chiswell, S.M., Middag, R., Laan, P., Sander, S.G., Koschinsky, A., 2022. Trace metal dynamics in shallow hydrothermal plumes at the Kermadec arc. Front. Mar. Sci. 8.
- Kletzin, A., Adams, M.W., 1996. Tungsten in biological systems. FEMS Microbiol. Rev. 18 (1), 5–63.
- Kojima, S., Sugaki, A., 1985. Phase relations in the Cu-Fe-Zn-S system between 500 degrees and 300 degrees C under hydrothermal conditions. Econ. Geol. 80 (1), 158-171.
- Kong, X.Z., Tutolo, B.M., Saar, M.O., 2013. DBCreate: a SUPCRT92-based program for producing EQ3/6, TOUGHREACT, and GWB thermodynamic databases at userdefined T and P. Comput. Geosci. 51, 415–417.
- Larson, B.I., Olson, E.J., Lilley, M.D., 2007. In situ measurement of dissolved chloride in high temperature hydrothermal fluids. Geochim. Cosmochim. Acta 71 (10), 2510–2523.
- Leigh, J.A., 2000. Nitrogen fixation in methanogens: the archaeal perspective. Curr. Issues Mol. Biol. 2 (4), 125–131.
- Lilley, M.D., Butterfield, D.A., Olson, E.J., Lupton, J.E., Macko, S.A., McDuff, R.E., 1993. Anomalous CH₄ and NH₄⁺ concentrations at an unsedimented mid-ocean-ridge hydrothermal system. Nature 364 (6432), 45–47.
- Liu, W., Etschmann, B., Mei, Y., Guan, Q., Testemale, D., Brugger, J., 2020. The role of sulfur in molybdenum transport in hydrothermal fluids: insight from in situ synchrotron XAS experiments and molecular dynamics simulations. Geochim. Cosmochim. Acta 290, 162–179.
- McDermott, J.M., Sylva, S.P., Ono, S., German, C.R., Seewald, J.S., 2018. Geochemistry of fluids from Earth's deepest ridge-crest hot-springs: Piccard hydrothermal field, Mid-Cayman Rise. Geochim. Cosmochim. Acta 228, 95–118.
- Metz, S., Trefry, J.H., 2000. Chemical and mineralogical influences on concentrations of trace metals in hydrothermal fluids. Geochim. Cosmochim. Acta 64 (13), 2267, 2270
- Miller, C.A., Peucker-Ehrenbrink, B., Walker, B.D., Marcantonio, F., 2011. Re-assessing the surface cycling of molybdenum and rhenium. Geochim. Cosmochim. Acta 75 (22), 7146–7179.
- Minubayeva, Z., Seward, T.M., 2010. Molybdic acid ionisation under hydrothermal conditions to $300\,^{\circ}$ C. Geochim. Cosmochim. Acta 74 (15), 4365–4374.
- Moore, E.K., Jelen, B.I., Giovannelli, D., Raanan, H., Falkowski, P.G., 2017. Metal availability and the expanding network of microbial metabolisms in the Archaean eon. Nat. Geosci. 10 (9), 629–636.

- Moore, E.K., Hao, J., Prabhu, A., Zhong, H., Jelen, B.I., Meyer, M., Hazen, R.M., Falkowski, P.G., 2018. Geological and chemical factors that impacted the biological utilization of cobalt in the Archean eon. J. Geophys. Res., Biogeosci. 123 (3), 743–759.
- Neumann, H., Mead, J., Vitaliano, C.J., 1954. Trace element variation during fractional crystallization as calculated from the distribution law. Geochim. Cosmochim. Acta 6 (2–3), 90–99.
- Nishioka, J., Obata, H., Tsumune, D., 2013. Evidence of an extensive spread of hydrothermal dissolved iron in the Indian Ocean. Earth Planet. Sci. Lett. 361, 26–33.
- Nitschke, W., Russell, M.J., 2009. Hydrothermal focusing of chemical and chemiosmotic energy, supported by delivery of catalytic Fe, Ni, Mo/W, Co, S and Se, forced life to emerge. J. Mol. Evol. 69 (5), 481–496.
- Pester, N.J., Rough, M., Ding, K., Seyfried, W.E., 2011. A new Fe/Mn geothermometer for hydrothermal systems: Implications for high-salinity fluids at 13 N on the East Pacific Rise. Geochim. Cosmochim. Acta 75 (24), 7881–7892.
- Ramondenc, P., Germanovich, L.N., Lowell, R.P., 2008. Modeling hydrothermal response to earthquakes at oceanic spreading centers. In: Lowell, R.P., Seewald, J.S., Metaxas, A., Perfit, M.R. (Eds.), Magma to Microbe: Modeling Hydrothermal Processes at Oceanic Spreading Centers. In: Washington DC American Geophysical Union Geophysical Monograph Series, vol. 178, pp. 97–121.
- Raymond, J., Siefert, J.L., Staples, C.R., Blankenship, R.E., 2004. The natural history of nitrogen fixation. Mol. Biol. Evol. 21 (3), 541–554.
- Robie, R.A., Hemingway, B.S., 1995. Thermodynamic Properties of Minerals and Related Substances at 298.15 K and 1 Bar (105 Pascals) Pressure and at Higher Temperatures (No. 2131). US Government Printing Office.
- Resing, J.A., Sedwick, P.N., German, C.R., Jenkins, W.J., Moffett, J.W., Sohst, B.M., Tagliabue, A., 2015. Basin-scale transport of hydrothermal dissolved metals across the South Pacific Ocean. Nature 523 (7559), 200–203.
- Robigou, V., Delaney, J.R., Stakes, D.S., 1993. Large massive sulfide deposits in a newly discovered active hydrothermal system, the High-Rise field, Endeavour segment, Juan de Fuca Ridge. Geophys. Res. Lett. 20 (17), 1887–1890.
- Roshan, S., Wu, J., Jenkins, W.J., 2016. Long-range transport of hydrothermal dissolved Zn in the tropical South Pacific. Mar. Chem. 183, 25–32.
- Roué, L., Kurzweil, F., Wille, M., Wegwerth, A., Dellwig, O., Münker, C., Schoenberg, R., 2021. Stable W and Mo isotopic evidence for increasing redox-potentials from the Paleoarchean towards the Paleoproterozoic deep ocean. Geochim. Cosmochim. Acta 309, 366–387.
- Saito, M.A., Sigman, D.M., Morel, F.M., 2003. The bioinorganic chemistry of the ancient ocean: the co-evolution of cyanobacterial metal requirements and biogeochemical cycles at the Archean-Proterozoic boundary? Inorg. Chim. Acta 356, 308–318.
- Sander, S.G., Koschinsky, A., 2011. Metal flux from hydrothermal vents increased by organic complexation. Nat. Geosci. 4 (3), 145–150.
- Schine, C.M., Alderkamp, A.C., van Dijken, G., Gerringa, L.J., Sergi, S., Laan, P., van Haren, H., van der Poll, W.H., Arrigo, K.R., 2021. Massive Southern Ocean phytoplankton bloom fed by iron of possible hydrothermal origin. Nat. Commun. 12 (1), 1–11.
- Schmidt, K., Koschinsky, A., Garbe-Schönberg, D., de Carvalho, L.M., Seifert, R., 2007. Geochemistry of hydrothermal fluids from the ultramafic-hosted Logatchev hydrothermal field, 15 N on the Mid-Atlantic Ridge: temporal and spatial investigation. Chem. Geol. 242 (1–2), 1–21.
- Schmidt, K., Garbe-Schönberg, D., Koschinsky, A., Strauss, H., Jost, C.L., Klevenz, V., Königer, P., 2011. Fluid elemental and stable isotope composition of the Nibelungen hydrothermal field (8 18' S, Mid-Atlantic Ridge): constraints on fluid-rock interaction in heterogeneous lithosphere, Chem. Geol. 280 (1–2), 1–18.
- Schwartz, M.O., 2000. Cadmium in zinc deposits: economic geology of a polluting element. Int. Geol. Rev. 42 (50). https://doi.org/10.1080/00206810009465091.
- SCOR Working Group, 2007. GEOTRACES—an international study of the global marine biogeochemical cycles of trace elements and their isotopes. Geochemistry 67 (2), 85–131.
- Scott, C., Lyons, T.W., Bekker, A., Shen, Y., Poulton, S.W., Chu, X., Anbar, A.D., 2008. Tracing the stepwise oxygenation of the Proterozoic ocean. Nature 452, 456–459.
- Shock, E.L., Sassani, D.C., Willis, M., Sverjensky, D.A., 1997. Inorganic species in geologic fluids: correlations among standard molal thermodynamic properties of aqueous ions and hydroxide complexes. Geochim. Cosmochim. Acta 61 (5), 907–950.
- Seewald, J.S., Seyfried, W.E., 1990. The effect of temperature on metal mobility in subseafloor hydrothermal systems: constraints from basalt alteration experiments. Earth Planet. Sci. Lett. 101 (2–4), 388–403.
- Seewald, J.S., Doherty, K.W., Hammar, T.R., Liberatore, S.P., 2002. A new gas-tight isobaric sampler for hydrothermal fluids. Deep-Sea Res., Part 1, Oceanogr. Res. Pap. 49 (1), 189–196.
- Seewald, J., Cruse, A., Saccocia, P., 2003. Aqueous volatiles in hydrothermal fluids from the Main Endeavour Field, northern Juan de Fuca Ridge: temporal variability following earthquake activity. Earth Planet. Sci. Lett. 216 (4), 575–590.
- Seyfried, W.E., 1987. Experimental and theoretical constraints on hydrothermal alteration processes at mid-ocean ridges. Annu. Rev. Earth Planet. Sci. 15 (1), 317–335.

- Seyfried, W.E., Ding, K., 1993. The effect of redox on the relative solubilities of copper and iron in Cl-bearing aqueous fluids at elevated temperatures and pressures: an experimental study with application to subseafloor hydrothermal systems. Geochim. Cosmochim. Acta 57 (9), 1905–1917.
- Seyfried, W.E., Ding, K., Rao, B., 2002. Experimental calibration of metastable plagioclase-epidote-fluid equilibria at elevated temperatures and pressures: Applications to the chemistry of hydrothermal fluids at mid-ocean ridges. In: Hellman, Roland, Wood, Scott A. (Eds.), Water-Rock Interactions, Ore Deposits, and Environmental Geochemistry: A Tribute to David A. Crerar. The Geochemical Society, pp. 257–278. Special Publication No. 7.
- Seyfried, W.E., Seewald, J.S., Berndt, M.E., Ding, K., Foustoukos, D.I., 2003. Chemistry of hydrothermal vent fluids from the Main Endeavour Field, northern Juan de Fuca Ridge: geochemical controls in the aftermath of June 1999 seismic events. J. Geophys. Res., Solid Earth 108 (B9).
- Seyfried, W.E., Tan, C., Wang, X., Wu, S., Evans, G.N., Coogan, L.A., Mihaly, S.F., Lilley, M.D., 2022. Time series of hydrothermal vent fluid chemistry at Main Endeavour Field, Juan de Fuca Ridge: remote sampling using the NEPTUNE cabled observatory. Deep-Sea Res., Part 1, Oceanogr. Res. Pap., 103809.
- Shang, L., Williams-Jones, A.E., Wang, X., Timofeev, A., Hu, R., Bi, X., 2020. An experimental study of the solubility and speciation of MoO3 (s) in hydrothermal fluids at temperatures up to 350°C. Econ. Geol. 115 (3), 661–669.
- Shvarov, Y.V., 2008. HCh: new potentialities for the thermodynamic simulation of geochemical systems offered by Windows, Geochem, Int. 46 (8), 834.
- Sippel, D., Einsle, O., 2017. The structure of vanadium nitrogenase reveals an unusual bridging ligand. Nat. Chem. Biol. 13 (9), 956–960.
- Sohn, R.A., Fornari, D.J., Von Damm, K.L., Hildebrand, J.A., Webb, S.C., 1998. Seismic and hydrothermal evidence for a cracking event on the East Pacific Rise crest at 9 50' N. Nature 396 (6707), 159–161.
- Stiefel, E.I., Coucouvanis, D., Newton, W.E., 1993. Molybdenum Enzymes, Cofactors, and Model Systems. ACS Publications.
- Tagirov, B.R., Seward, T.M., 2010. Hydrosulfide/sulfide complexes of zinc to 250 C and the thermodynamic properties of sphalerite. Chem. Geol. 269 (3-4), 301-311
- Tagliabue, A., Bopp, L., Dutay, J.C., Bowie, A.R., Chever, F., Jean-Baptiste, P., Bucciarelli, E., Lannuzel, D., Remenyi, T., Sarthou, G., Aumont, O., Gehlen, M., Jeandel, C.,

- 2010. Hydrothermal contribution to the oceanic dissolved iron inventory. Nat. Geosci. 3 (4), 252–256.
- Tivey, M.K., Delaney, J.R., 1986. Growth of large sulfide structures on the Endeavour Segment of the Juan de Fuca Ridge. Earth Planet. Sci. Lett. 77 (3–4), 303–317.
- Tivey, M.K., Stakes, D.S., Cook, T.L., Hannington, M.D., Petersen, S., 1999. A model for growth of steep-sided vent structures on the Endeavour Segment of the Juan de Fuca Ridge: results of a petrologic and geochemical study. J. Geophys. Res., Solid Earth 104 (B10), 22859–22883.
- Trefry, J.H., Butterfield, D.B., Metz, S., Massoth, G.J., Trocine, R.P., Feely, R.A., 1994. Trace metals in hydrothermal solutions from Cleft segment on the southern Juan de Fuca Ridge. J. Geophys. Res., Solid Earth 99 (B3), 4925–4935.
- Von Damm, K.L., Edmond, J.M., Grant, B., Measures, C.I., Walden, B., Weiss, R.F., 1985. Chemistry of submarine hydrothermal solutions at 21 °N, East Pacific Rise. Geochim. Cosmochim. Acta 49 (11), 2197–2220.
- Vorlicek, T.P., Kahn, M.D., Kasuya, Y., Helz, G.R., 2004. Capture of molybdenum in pyrite-forming sediments: role of ligand-induced reduction by polysulfides. Geochim. Cosmochim. Acta 68 (3), 547–556.
- Weiss, M.C., Sousa, F.L., Mrnjavac, N., Neukirchen, S., Roettger, M., Nelson-Sathi, S., Martin, W.F., 2016. The physiology and habitat of the last universal common ancestor. Nat. Microbiol. 1 (9), 1–8.
- Wilcock, W.S., 2004. Physical response of mid-ocean ridge hydrothermal systems to local earthquakes. Geochem. Geophys. Geosyst. 5 (11).
- Wille, M., Nebel, O., Van Kranendonk, M.J., Schoenberg, R., Kleinhanns, I.C., Ell-wood, M.J., 2013. Mo-Cr isotope evidence for a reducing Archean atmosphere in 3.46–2.76 Ga black shales from the Pilbara, Western Australia. Chem. Geol. 340, 68–76.
- Williams, R.J.P., Rickaby, R.E., 2012. Evolution's Destiny: Co-Evolving Chemistry of the Environment and Life. Royal Society of Chemistry.
- Wu, J., Wells, M.L., Rember, R., 2011. Dissolved iron anomaly in the deep tropicalsubtropical Pacific: evidence for long-range transport of hydrothermal iron. Geochim. Cosmochim. Acta 75 (2), 460–468.
- Xing, Y., Brugger, J., Sheuermann, P., Tan, C., Ji, S., Seyfried, W.E., 2022. An experimental and thermodynamic study of sphalerite solubility in chloride-bearing fluids at 300-450 °C, 500 bar: implications for zinc transport in seafloor hydrothermal systems. Geochim. Cosmochim. Acta.